Estimating resist parameters in optical lithography using the extended Nijboer-Zernike theory

Peter Dirksen
Philips Research Leuven
Kapeldreef 75
B-3001 Leuven, Belgium
E-mail: peter.dirksen@philips.com

Joseph Braat
Delft University of Technology
Faculty of Applied Sciences
Optics Research Group
Lorentzweg 1
NL-2628 CJ Delft
The Netherlands

Augustus J. E. M. Janssen
Philips Research Laboratories
WO-02
NL-5656 AA Eindhoven
The Netherlands

Abstract. This study presents an experimental method to determine the resist parameters at the origin of a general blurring of a projected aerial image. The resist model includes the effects of diffusion in the horizontal plane and image blur that originates from a stochastic variation of the focus parameter. We restrict ourselves to the important case of linear models, where the effects of resist processing and focus noise are described by a convolution operation. These types of models are also known as diffused aerial image models. The used mathematical framework is the so-called extended Nijboer-Zernike (ENZ) theory, which allows us to obtain analytical results. The experimental procedure to extract the model parameters is demonstrated for several 193-nm resists under various conditions of postexposure baking temperatures and baking times. The advantage of our approach is a clear separation between the optical parameters, such as feature size, projection lens aberrations, and the illuminator setting on one hand, and process parameters introducing blur on the other. © 2006 Society of Photo-Optical Instrumentation Engineers. [DOI: 10.1117/1.2168449]

Subject terms: optical lithography; resist; diffusion constant; focus noise; point-spread function; extended Nijboer-Zernike theory.

Paper 05041R received Jun. 6, 2005; revised manuscript received Oct. 20, 2005; accepted for publication Oct. 23, 2005; published online Feb. 2, 2006. This paper is a revision of a paper presented at the SPIE conference on Optical Microlithography XVII, Feb. 2004, Santa Clara, California. The paper presented there appeared (unrefereed) in the SPIE proceedings Vol. 5377.

1 Introduction

Currently, optical lithography is able to print sub-40-nm lines using a binary mask and advanced resist processing.[1] The line width is of the same order of magnitude as the image blur caused by the effects of acid diffusion. In addition the depth of focus, about 300 nm is of the same order of magnitude as the stochastic variation of the focus parameter. An extended diffused aerial image model is a simple but powerful method to take these image blur effects into account.

The influence of longitudinal and transverse vibrations on the transfer function is described in Ref. 2. It was shown that both vibrations have a degrading effect on the image quality. For a step and scan system, the effects of image blur in the horizontal plane are described in Refs. 3–5. Here, image blur originates from mechanical noise and synchronization errors. A probability density function was used to describe the statistics of the disturbance. Mathematically, a convolution of the probability density function with the static aerial image is used to calculate a diffused aerial image. The influence of the finite resist thickness is described in Ref. 6 as an integral of the aerial image over the resist thickness. The application of a diffused aerial image to optical proximity corrections is described in Ref. 7, where a Gaussian probability density function is used to describe the effects of acid diffusion during the postexposure baking (PEB) process. In various publications, the validity of the diffused aerial image model (DAIM) was assessed.[8,9] It was concluded that DAIM is a good predictor not only for lines and spaces, but also for 2-D structures such as contact holes. The accuracy of DAIM was found to be comparable to full resist models.

In this study, we describe an extension of the DAIM model. Not only do we include the effects of diffusion in the horizontal plane, but also a second cause for image blur that originates from a stochastic variation of the focus parameter. Therefore, both the radial coordinate r and focal coordinate f are treated as a stochastic parameter with a standard deviation σ_r and σ_f, respectively. The two parameters describe the transition from aerial image to resist image; therefore, we call σ_r and σ_f the resist parameters of the extended diffused aerial image model.

To estimate the resist parameters, it is our first task to make a clear distinction between optical parameters, such as feature size, projection lens aberrations, and the illuminator setting on one hand, and resist parameters on the other. For this purpose, we use the extended Nijboer-Zernike (ENZ) aberration retrieval method, which is designed for retrieving aberrations from the through-focus intensity point-spread function.[10–14] The used mathematical framework is presented, and the experimental procedure to extract the resist parameters is demonstrated. The experimental procedure involves the analysis of a focus-exposure

1537-1646/2006/$22.00 © 2006 SPIE

matrix of an isolated contact hole. The results of several 193-nm resists under various conditions of PEB temperatures and baking times are shown. For our experiments, we use a modern 193-nm wafer scanner.

The work is organized as follows. Section 2 describes the used mathematical background of the aberrated point-spread function in the presence of diffusion in the horizontal plane and image blur that originates from a stochastic variation of the focus parameter. Section 3 describes the procedure to retrieve the resist parameters from a through-focus intensity point-spread function. The procedure is tested on numerically simulated diffused aerial images. Section 4 presents the experimental results obtained on several 193-nm resists under various conditions. For applications with a high geometrical imaging aperture, also encountered in immersion lithography, a full vectorial treatment of the point-spread function is needed. Some aspects of the extended Nijboer-Zernike approach for the ultra-high NA applications are discussed in Sec. 5. Appendix A in Sec. 7 gives the relationship between normalized image coordinates (x,y) and the defocus parameter f on one hand, and the real space image coordinates (X,Y,Z) in the lateral and axial direction on the other. Appendix B in Sec. 8 gives the correction of the basic diffraction integrals for a non-negligible hole size. Appendix C in Sec. 9 gives the additional correction terms that are needed to incorporate the lateral and axial blurring effects in the aberration retrieval scheme.

2 Mathematical Framework

2.1 *Resist Models*

Full resist models are essentially nonlinear models. In the exposed areas of a chemically amplified resist (CAR), acid is generated that diffuses during the postexposure baking (PEB) process.[15,16] In addition, a chemical base or quencher reacts with the acid and influences the final acid distribution. The development process[17] and the metrology tool also influence the shape of the observed resist profile. Finally, there is a nonzero resist thickness, finite resist contrast, and nonzero resist absorption. The combination of all these effects have an impact on the lateral dimensions of the observed resist profile. Full resist models can include these effects accurately, but are in general hard to calibrate due to the large number of model parameters involved.

Diffused aerial image models approximate resist processing, mechanical, metrology, and optical blur effects by assuming linearity: the combined blur effect is described by a convolution operation of the aerial image with a certain kernel. This is the approach we take in our work.

On top of the blur effects described before, wafer stage noise in the (X,Y) direction contributes to blur in the horizontal plane of the projected aerial image as well. In our model, the combined effect is described by a single diffusion parameter σ_r. A second cause for image blur originates from a stochastic variation of the focus parameter. Wafer stage noise in the Z direction and the finite bandwidth of the laser source $\Delta\lambda$, combined with chromatic aberrations of the projection lens, contribute to the statistical variation around the optimal focus.[18] In our model, the combined effect is described by a single focus noise parameter σ_f. For a step and scan system, there are additional sources of image blur[3] related to the scanning motion of the wafer and reticle stage, such as synchronization errors. Also, distortion and field curvature contribute to blur as the point-spread function is scanned through the field of the projection lens. The defocus value of the pinhole image will thus vary during the exposure in case of field curvature. In other words, the impact of field curvature on the observed point-spread function (PSF) is similar to focus noise. Likewise, distortion causes the pinhole image to make an excursion in the XY plane during the scan and thus contributes to blur in the horizontal planes.

There is a category of photoresists where the linear approach is sufficiently accurate. For these resists, the linear DAIM models perform equally well as the full resist models[8,9,19,20] in terms of predicting top-down CD values for a variety of features, pitch values, and imaging conditions. We note that although we assume Gaussian distribution functions for simplicity, the shape of the convolution kernel is not essential and could be generalized.[20]

2.2 *Basic Expressions Used in the Extended Nijboer-Zernike Theory*

Next, we describe the extended Nijboer-Zernike theory to calculate the intensity point-spread function in the presence of diffusion and focus noise. For small values of the diffusion parameter and focus noise parameter, we obtain analytical results that allow us to retrieve the resist parameters. The point-spread function or impulse response[21] of an optical system is the image of an infinitely small object. In practice, an object having a diameter of the order $\sim\lambda/2\mathrm{NA}$ is a fair approximation, and then the finite hole size has to be taken into account (see Appendix B in Sec. 8). The complex amplitude of the point-spread function is denoted as $U(x,y)$, with (x,y) being the coordinates scaled to the ratio of wavelength and numerical aperture. Also, we assume a rotationally symmetrical blur function. It is sufficient for our purpose to consider only the rotationally symmetrical terms $(m=0)$ of the intensity point-spread function. In our restricted analysis, only the radial and axial blur effects are included in the $\beta_{n,0}$-coefficients [see Eq. (1)].

For a good lens having small radially symmetric transmission variations and phase errors, the pupil function is written as:

$$A(\rho)\cdot\exp\{i\Phi(\rho)\}=\sum_{p}\beta_{2p,0}Z_{2p}^{0}(\rho), \tag{1}$$

with A being the amplitude pupil transmission function and Φ the pupil phase function, and Z_{2p}^{0} the radially symmetric Zernike terms. According to the ENZ theory, for small aberrations ($A\approx 1$ and $|\Phi|\ll 1$),

$$I\approx 4\beta_{0,0}^{2}|V_{0}^{0}|^{2}+\beta_{0,0}\sum_{p\neq 0}[\mathrm{Im}(\beta_{2p,0})\Psi_{2p}^{0}+\mathrm{Re}(\beta_{2p,0})\chi_{2p}^{0}], \tag{2}$$

where the intensity is written as a linear summation of basic functions $\chi_{2p}^{0},\Psi_{2p}^{0}$. For small aberrations, the Ψ_{2p}^{0} terms correspond to the phase errors, and the χ_{2p}^{0} terms correspond to the amplitude errors. The projection lens aberrations manifest themselves as coefficients $\beta_{n,m}$ of the basic functions:

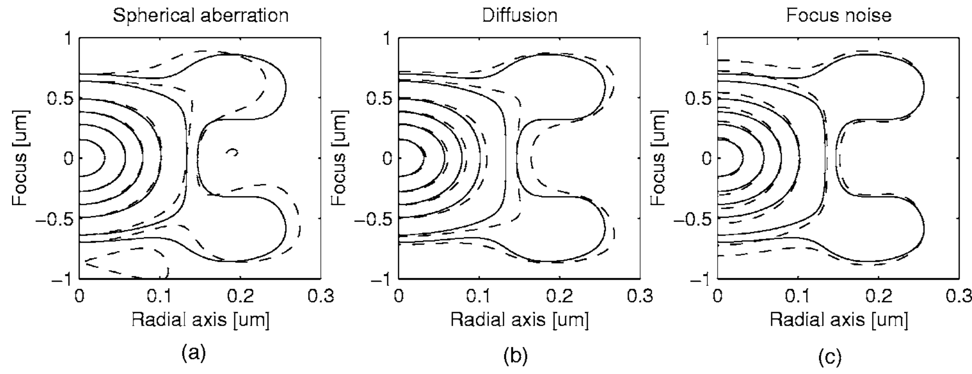

Fig. 1 Contour plots of the intensity point-spread function $I(r,f)$ showing the influence of spherical aberration, diffusion, and focus noise on an aberration-free intensity point-spread function (solid lines) for $\lambda = 193$ nm and NA=0.63. The six contours are lines of equal intensity in the range from [0.05, 0.1, 0.3, 0.5, 0.7, 0.9] of the maximum intensity: (a) with $Z_9 = 75m\lambda$ spherical aberration (dashed lines), (c) with $\sigma_r = 30$-nm diffusion (dashed lines), and (c) with $\sigma_f = 150$-nm focus noise (dashed lines). Note that the influences of spherical, diffusion, and focus noise are rather different.

$$\chi_n^m(r,f) = \gamma_m \operatorname{Re}\{i^m V_0^{0*} V_n^m\}$$

$$\Psi_n^m(r,f) = \gamma_m \operatorname{Re}\{i^{m+1} V_0^{0*} V_n^m\}, \tag{3}$$

with $\gamma_m = 4$, $m = 1, 2, \ldots$, and $\gamma_0 = 8$. Since we restrict ourselves to radial symmetry, only $m = 0$ and $n = 2p$ occur. Appendix A in Sec. 7 gives the definitions of the scaled coordinates as well as the definition of the radial functions $V_{n,m}$.

2.3 *Influence of Projection Lens Aberrations*

Using the results from Eqs. (2) and (3), the intensity point-spread function in the presence of spherical aberration is given by:

$$I(r,f) = |V_0^0|^2 + 2\operatorname{Im}(\beta_{2p,0})\operatorname{Re}\{iV_0^{0*}V_{2p}^0\}. \tag{4}$$

Figure 1(a) illustrates the intensity point-spread function when a certain amount of low order spherical aberration ($p = 2$) is included. In the case of "no diffusion" and "no focus noise," the $\beta_{2p,0}$-coefficients can be estimated by applying a matching procedure to Eq. (2). The details of this procedure are published elsewhere.[13]

2.4 *Diffusion and Focal Noise*

We now consider the effects of blur in the through-focus image planes and of focal noise on the recorded intensity, and discuss corrections of the basic functions in the retrieval scheme for these effects.

Blur in the image planes arises in two different ways. The first blur cause is position noise. For mechanical Gaussian noise in the horizontal plane (isotropic, without preferred direction), we have a Gaussian probability density function (pdf) of the type:

$$d(x,y) = \frac{1}{2\pi\sigma^2}\exp\left(-\frac{x^2+y^2}{2\sigma^2}\right), \tag{5}$$

with $\sigma = \sigma_m$ the standard deviation of the mechanical noise. The blurred image is obtained by a 2-D convolution of the static image intensity $I(x,y,f)$ and the pdf:

$$I'(x,y,f) = \int_{-\infty}^{\infty}\int_{-\infty}^{\infty} I(x',y',f)\,d(x-x',y-y')\,\mathrm{d}x'\mathrm{d}y'. \tag{6}$$

Examples of various other pdfs describing sinusoidal vibrations, distortion averaging, and synchronization errors are described elsewhere.[3]

A second cause for blur in the image plane is acid diffusion during the postexposure baking process. The effect on the recorded intensity is again a 2-D convolution with a Gaussian pdf as in Eq. (5), where the standard deviation $\sigma = \sigma_c$ is interpreted as the Fickian diffusion length,

$$\sigma_c = \sqrt{2Dt}, \tag{7}$$

with D the acid diffusion coefficient and t the baking time.

Under the condition of independent mechanical and chemical causes for blur in the image planes, the total effect can be described by Eqs. (5) and (6) with

$$\sigma = \sigma_r = \sqrt{\sigma_m^2 + \sigma_c^2}. \tag{8}$$

We next consider image blur caused by stochastic variation of the focus parameter f. This effect can be taken into account by convolving the intensity $I(x,y,f)$ in the focal direction with a Gaussian pdf

$$f_n(f) = \frac{1}{\sigma_f\sqrt{2\pi}}\exp\left(-\frac{f^2}{2\sigma_f^2}\right), \tag{9}$$

according to

$$I'(x,y,f) = \int_{-\infty}^{\infty} I(x,y,f')\,f_n(f-f')\,\mathrm{d}f', \tag{10}$$

where σ_f is the standard deviation of the focal noise.

Assuming the blurring process in the image planes and in the focal direction to be independent from one another, the total effect on the image intensity is given by the formula

$$I'(x,y,f) = \int_{-\infty}^{\infty}\int_{-\infty}^{\infty}\int_{-\infty}^{\infty} I(x',y',f')d(x-x',y-y') \times f_n(f-f')\mathrm{d}x'\mathrm{d}y'\mathrm{d}f'. \quad (11)$$

Here, $d(x,y)$ is given by the right-hand side of Eq. (5), with $\sigma=\sigma_r$ as in Eq. (8), and $f_n(f)$ is given by Eq. (9).

In Appendix C in Sec. 9 we present second-order corrections of the dominating basic functions $|V_0^0|^2$ and first-order corrections of the basic intensity functions Ψ_{2p}^0, χ_{2p}^0 in Eq. (2) to take the effect of blurring according to Eq. (11) into account. The formulas that arise are analytical in nature, and are especially useful for the case of small to medium-large values of σ_r and σ_f. This avoids the numerical calculation of the integrals at the right-hand side of Eq. (11), which is a time-consuming matter, especially when σ_r and or σ_f are small. Due to symmetry of the involved pdfs [see Eqs. (5) and (9)], the corrections presented in Appendix C in Sec. 9 for image blur in the spatial domain and in the focal direction are additive up to and including second order.

By way of illustration, we present the first-order corrected expression for $|V_0^0|^2$ with only spatial blur and focal noise. They are given, respectively, as

$$I(r,f) = |V_0^0|^2 - \pi^2\sigma_r^2 \cdot [2|V_0^0|^2 - 4|V_1^1|^2 + 2\,\mathrm{Re}(V_2^0 V_0^{0*})], \quad (12)$$

and

$$I(r,f) = |V_0^0|^2 - \frac{1}{2}\sigma_f^2\left[\frac{1}{6}|V_0^0|^2 - \frac{1}{2}|V_2^0|^2 + \frac{1}{3}\,\mathrm{Re}(V_4^0 V_0^{0*})\right]. \quad (13)$$

Figure 1 shows contour plots of the intensity point-spread function (PSF) $I(r,f)$, illustrating the influence of spherical aberration, diffusion, and focus noise on an aberration-free intensity point-spread function for $\lambda = 193$ nm and NA=0.63. The six contours represent lines of equal intensity in the range of [0.05, 0.1, 0.3, 0.5, 0.7, 0.9] of the maximum intensity. Figure 1(a) illustrates the intensity point-spread function when a certain amount of spherical aberration is included. Spherical aberration causes a through-focus asymmetry, i.e., $I(r,f) \neq I(r,-f)$. Figure 1(b) shows the diffused Airy pattern when diffusion with a nonzero variance σ_r is included. Diffusion stretches the PSF in the (X,Y) plane and causes a broadening or loss of resolution of the PSF. Figure 1(c) shows the diffused Airy pattern when focus noise with a nonzero variance σ_f is included. Focus noise stretches the PSF in the Z direction, almost without broadening it in the (X,Y) direction. This effect is known as focus drilling and causes an increase in depth of focus for the more isolated features at the expense of exposure latitude. Both diffusion and focus noise maintain the through-focus symmetry $I(r,f)=I(r,-f)$. The impact of spherical aberration, diffusion, and focus noise on the point-spread function is seen to be quite different. This effect can be understood as follows: the bracketed terms in Eqs. (12) and (13) have a rather different (r,f) dependence. The main reason is the function $|V_1^1(r,f)|^2$ that has a strong r dependence. This function is absent in Eq. (13), which implies that the effect of focus noise cannot be mimicked by a diffusion process. Further evidence can be found in

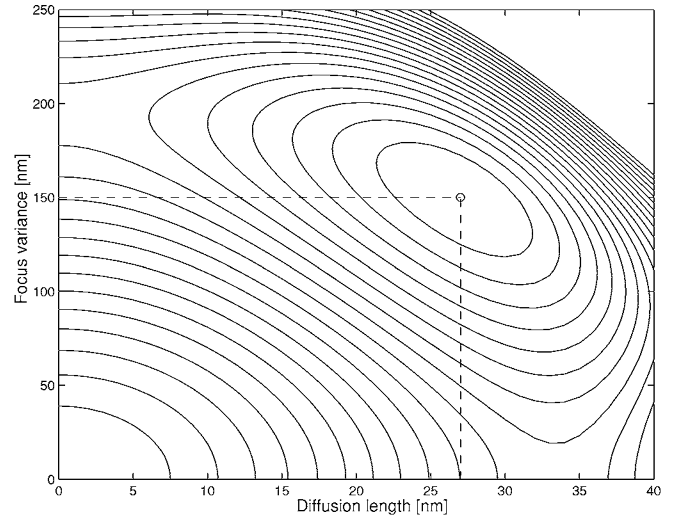

Fig. 2 Experimental result of the figure of merit $M(\sigma_r,\sigma_f)$ for contact hole resist. The minimum indicates a diffusion parameter σ_r =27 nm and a focus noise parameter σ_f=150 nm.

Fig. 2: the diffusion length found is to a large extent independent of the focus noise parameter and vice versa. Thus, one should be able to separate diffusion and focus noise experimentally.

3 Retrieving the Optical Parameters and Resist Parameters from the Intensity Point-Spread Function

The basic tool we use for estimating the resist parameters is aberration retrieval using the ENZ method, for which the measured intensity PSF is required. This method, described in detail in Ref. 22, is here briefly discussed. According to Eq. (2), the through-focus PSF is expressed as a combination of basic functions Ψ_{2p}^0, χ_{2p}^0. The complex coefficients $\beta_{2p,0}$ of these basic functions represent the pupil function, and are estimated by optimizing the match between the theoretical intensity and the measured intensity patterns at several values of the defocus parameter.

The ENZ method uses some elements of linear algebra. The resulting linear systems for the aberration coefficients are generically well conditioned due to near-orthogonality of the relevant basic functions. An inner product is defined in the (r,f) space:

$$(\Psi,\chi) = \int_0^R \int_{-F}^{F} r \cdot \Psi(r,f) \cdot \chi(r,f)^* \mathrm{d}r\mathrm{d}f. \quad (14)$$

When taking inner products in Eq. (2) with $\Psi_{2p'}^0$ and $\chi_{2p'}^0$, one should note that $\Psi_{2p'}^0$ and $\chi_{2p'}^0$ have opposite parity with respect to their dependence on f, so that their inner product vanishes. Thus, in the presence of both amplitude and phase errors, two sets of decoupled linear equations are to be solved.

We note the following.

- According to Eq. (2), the intensity point-spread function is a linear sum of basic intensity functions.

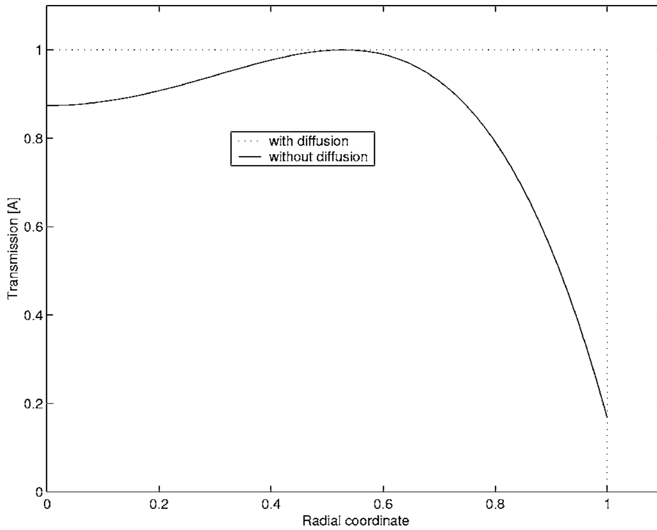

Fig. 3 Dashed line: reconstruction of a perfect pupil transmission function $A=1$ from the through-focus intensity PSF, blurred by diffusion and focus noise, using the corrected basic functions. Solid line: when diffusion or focus noise are ignored, a significant apparent transmission error results.

- Image blur, caused by a diffusion process or focus noise, is a linear process on the level of intensities.
- Therefore, we may "diffuse" the separate basic intensity functions and use "diffused basic intensity functions" in the ENZ formalism.
- The coefficients β of the diffused basic intensity functions represent the aberrations of the projection lens and can be found by a least-square fitting routine as described before. Aberration retrieval with or without diffusion or focus noise can therefore be achieved according to the same principle.

Figure 3 shows a simulated example of aberration retrieval in the presence of image blur. Using Eqs. (12) and (13), we have calculated the aberration-free intensity point-spread function including diffusion $\sigma_r=0.025\ \mu\text{m}$ and focus noise $\sigma_f=0.175\ \mu\text{m}$. Next, we retrieve the aberrations from this blurred PSF and pay particular attention to the aberration terms that describe a transmission error. Using the corrected basic intensity functions, including diffusion and focus noise, indeed an aberration-free pupil function with $A=1$ and $\Phi=0$ is reconstructed. However, if the incorrect basic functions (ignoring diffusion and focus noise) are used, a significant apparent transmission variation across the pupil of the lens is observed. In both cases, the reconstructed phase aberrations are zero. This effect can be understood as follows: our blur functions have rotational symmetry and through-focus symmetry. Therefore, the blurred image must have the same symmetry properties as the aberration-free, nonblurred image. However, diffusion and focus noise do broaden the aerial image in a specific way, as shown in Fig. 1. This broadening of the PSF can be approximated by assuming large transmission errors, but cannot be accounted for by assuming phase errors.

As a next step, we assume a high-quality lens with negligible transmissions errors and possibly non-negligible but small phase errors. Accordingly, $A(\rho)\approx 1$ and the $\text{Re}(\beta_{2p,0})$ in Eq. (1) should practically vanish. We define a figure of merit $M(\sigma_r,\sigma_f)$ for finding the resist parameters:

$$M(\sigma_r,\sigma_f)=\frac{\sum_{p\neq 0}\frac{1}{2(2p+1)}[\text{Re}(\beta_{2p,0})]^2}{\sum_{p}\frac{1}{2(2p+1)}\{[\text{Re}(\beta_{2p,0})]^2+[\text{Im}(\beta_{2p,0})]^2\}}, \tag{15}$$

representing the power in the transmission terms, normalized to the total power. For each value of (σ_r,σ_f), we determine the aberrations of the system, i.e., the β coefficients. The values of σ_r and σ_f that yield the minimum of M are the true values of DAIM, since they are maximally consistent with our assumption of dealing with a lens having negligible transmission errors.

We note that under our assumptions of having a high-quality lens and small parameters (σ_r,σ_f), the effects of diffusion and focus blur are additive. That means that in the presence of both effects, the terms in Eqs. (12) and (13) involving σ_r^2 and σ_f^2 simply add to the nonblurred point-spread function [see also Eq. (39)].

3.1 *Comparison with SOLID-C Simulation Results*

To validate the retrieval procedure, we retrieved the noise parameters from SOLID-C (Ref. 23) calculated diffused aerial images. Position and focus noise are both implemented in the lithographic simulator SOLID-C in the options "detailed scanner noise in (X,Y,Z)." The simulator uses the same settings as the experiments: the exposure wavelength is $\lambda=193$ nm and the numerical aperture is NA=0.63. For the optical model, we used the so-called high NA scalar transfer matrix model, aberration-free case. Next, we used the ENZ theory to retrieve the resist parameters from the simulated aerial image. Figure 4 illustrates the retrieval procedure. For each value of the diffusion parameter in the range 0 to 50 nm, we calculate the basic intensity functions taking the diffusion correction according to Eqs. (28), (31), and (34) of Appendix C in Sec. 9 into account.

We retrieve the β coefficients and calculate the figure of merit $M(\sigma_r)$. The argument of minimal $M(\sigma_r)$ corresponds to the retrieved diffusion parameter. In a similar way, the focus noise parameter can be obtained, taking the correction for focus noise according to Eq. (13) into account, by searching for the minimum of $M(\sigma_r,\sigma_f)$. In Table 1 we compare several examples of the SOLID-C input parameter with the retrieved parameters (σ_r,σ_f). The parameter values are relatively small compared to the 50% resolution of 80 nm and depth of focus of 400 nm. We observe that the effects of diffusion and focus noise indeed behave independently. The small differences between input and retrieved parameters correspond to very small intensity differences, well below 1% of the point-spread function.

4 Experimental Determination of Resist Parameters

This section describes the basic experiment to determine the resist parameters. The reticle is a simple chrome-on-quartz reticle with a $4\times 0.15=0.6$-μm-diam transparent

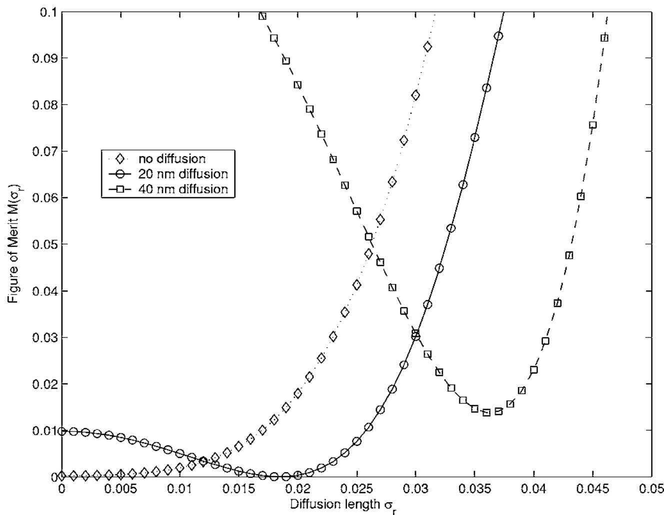

Fig. 4 Retrieval of the diffusion parameter of the SOLID-C generated aerial images. The figure of merit $M(\sigma_r)$ is shown as a function of the diffusion length. The minimum occurs at the true value of the diffusion parameter. Dotted lines, diamonds: no diffusion. Solid line, circles: the SOLID-C input value is 20 nm, and the retrieved diffusion parameter is σ_r=18 nm. Dashed line, squares: the SOLID-C input value is 40 nm, and the retrieved diffusion parameter is σ_r =36 nm.

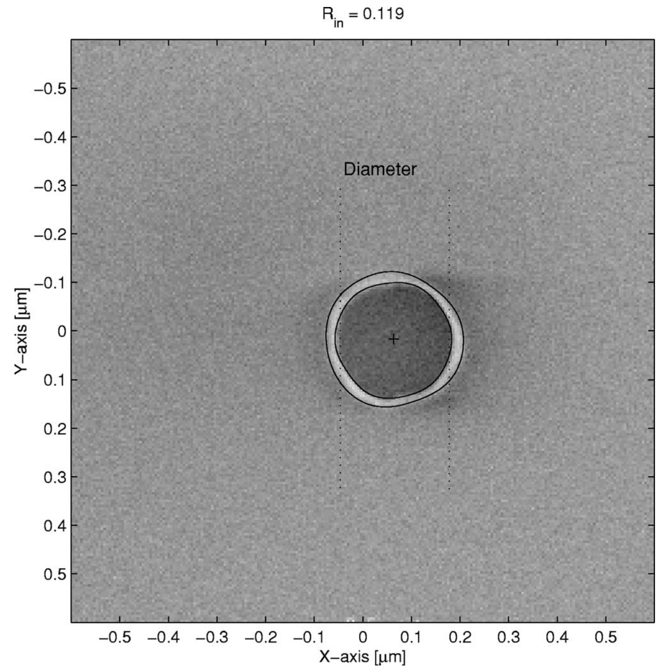

Fig. 5 An example of a single pinhole exposure. The diameter is defined as the inner diameter of the contact hole.

hole. An ASML PAS5500/950 system with a λ=193-nm, NA=0.63 projection lens is used to image the reticle onto resist on a SiON antireflective coating. Using SiON instead of an organic antireflective coating has the advantage of providing a good contrast in the scanning electron microscope (SEM). Next, we record a focus-exposure matrix of the isolated contact hole in photoresist, and measure the hole diameter in a SEM. A Hitachi 9200 CD-SEM, under job control, collects all images. The data reduction is done off-line. A typical example of a SEM image is shown in Fig. 5. We extract the inner diameter of the contact hole. This parameter corresponds to a slice of the diffused aerial image. The related intensity value in the aerial image scales as 1/(exposure dose). The focus-exposure matrix is thus interpreted as the through-focus intensity point-spread function of the projection lens. We note that no bias or additional parameters are involved. Figure 6 shows an example of a focus-exposure matrix of the contact hole and the corresponding point-spread function.

Figure 2 shows an experimental example of the figure of merit. The merit function shows a distinct minimum indicating a diffusion parameter σ_r=27 nm and a focus noise parameter σ_f=150 nm. We verify that, for optimal resist parameters, the transmission variation across the pupil of the lens is below 0.5%, in agreement with our assumption A=1. Figure 7 shows the resulting fit to the experimental data. The mean square relative error equals 1.9%.

Table 1 Comparison of several examples of the SOLID-C input parameter with retrieved parameters (σ_r, σ_f).

Input SOLID-C		Retrieved by ENZ	
σ_r [nm]	σ_f [nm]	σ_r [nm]	σ_f [nm]
0	0	0	0
20	0	18	0
40	0	36	0
0	100	0	100
0	200	0	200
10	50	7	50
20	100	18	100
40	200	39	180

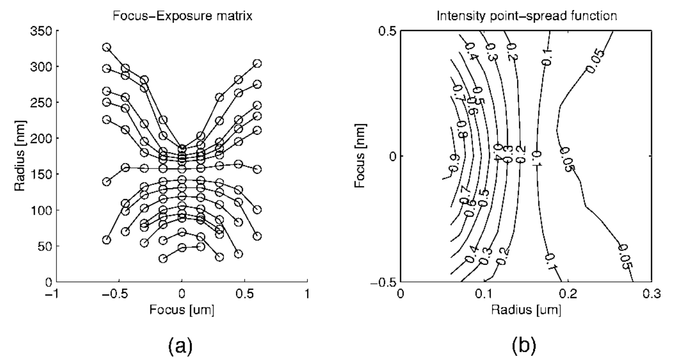

Fig. 6 (a) Focus-exposure matrix of an isolated contact hole. The radius of the developed resist contour as a function of the focus setting; the parameter yielding the set of curves is the exposure dose, ranging from 20 to 800 mJ/cm^2. (b) A contour plot of the intensity point-spread function of the projection lens in a cross section containing the vertical axis. The data of the focus-exposure matrix is used.

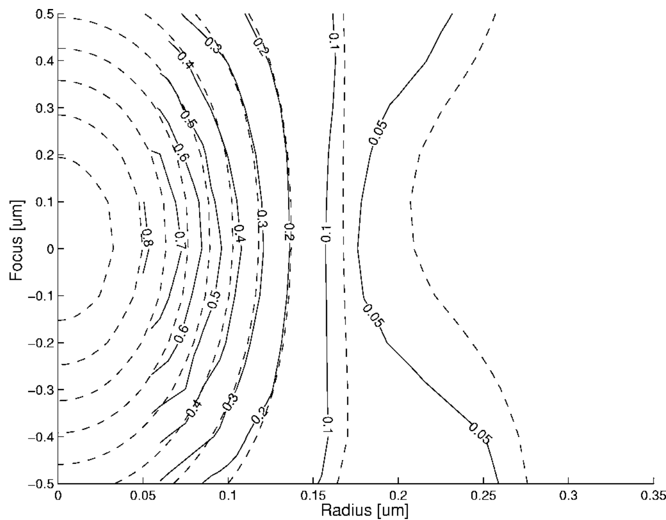

Fig. 7 Contour plot of the experimental intensity point-spread function (solid lines) compared to the data fit (dashed lines) for ARX 1561J resist, using the optimal parameter (σ_r=27, σ_f=150).

4.1 *Experimental Results for Various Resists under Various Conditions*

Figure 8(a) shows the dependence of the measured diffusion length σ_r on the postexposure baking temperature for two resists. The standard resist has a larger diffusion parameter and steeper temperature dependence compared to the low PEB-sensitive resist. The increase of σ_r reflects the expected increase of acid diffusion length versus baking temperature. Figure 8(b) shows PEB time dependence for the standard resist. The solid curve is a fit to the experimental data, assuming an $\sqrt{2D\cdot t+\text{offset}}$ increase of the diffusion parameter with time. The mean square error of the experimental data with respect to the fitted curve is 1.6 nm.

Figure 9 summarizes our results of diffusion and focus noise measurements. The diffusion parameter measurements of different resists are summarized in Fig. 9(a). We have included the results of contact hole resist (A), a low PEB-sensitive resist (B), our "standard" resist (C), and also the result for a 157-nm resist (E) that has been exposed on the 193 scanner. This result indicates that the model can be calibrated for various resist types and chemistries. The validity and predictiveness of diffused aerieal image models to other structures or illumination conditions were assessed elsewhere.[8,9] The contact hole resist has clearly the smallest diffusion length. In an additional experiment, the resist vendor has modified the standard resist on request and replaced the photoacid generator (PAG) anion by a smaller one. The modified resist is indicated as resist (D). This resulted in a release of smaller acid molecules and was expected to cause a significant increase of the diffusion parameter, in agreement with the experimental result.

The focus noise parameter measurements of all the data points of various resists processed under various conditions are summarized in Fig. 9(b). As expected, focus noise is independent of the resist type or process condition. The mean focus noise value is 189 nm, as indicated by the dashed line. The standard deviation is 12 nm. Possible sources that contribute to the observed focus noise are the laser bandwidth combined with the chromatic aberrations of the lens, Z noise of the wafer stage, and, for the scanner, field curvature.

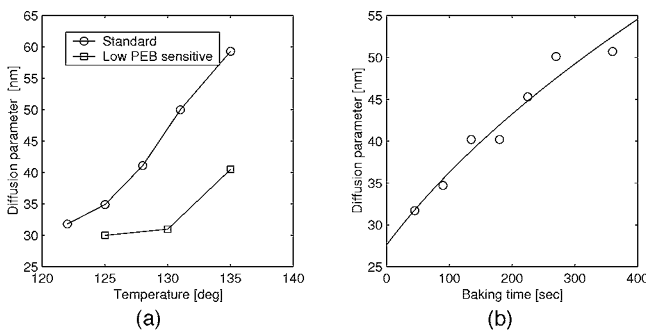

Fig. 8 (a). The dependence of the diffusion parameter σ_r on the PEB temperature. The solid lines serve as a visual guideline. (b) The dependence of the diffusion parameter σ_r on the baking time of the PEB. Here, the solid line represents the $\sqrt{2D\cdot t+\text{offset}}$ dependence. Both measurements reflect the expected increase of acid diffusion of a chemically amplified resist with PEB time and temperature.

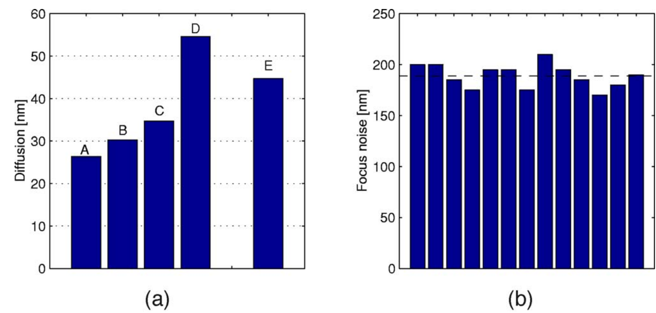

Fig. 9 (a) Diffusion parameter σ_r for various resist types. Exposures were made under nominal conditions of PEB time and PEB temperature. The contact hole resist (A) shows the smallest diffusion length. Resist (B) is a low PEB-sensitive resist. Resist (D) is a modified version of the standard resist (C), containing a smaller PAG. The 157-nm resist (E) is exposed on the λ=193-nm scanner. (b) A summary of the focus noise parameter for all resists and process conditions. The mean value of 189 nm is indicated by the dashed line.

5 Outlook

5.1 *Anisotropic Diffusion*

We have restricted ourselves to a rotationally symmetrical blur function. Thus, it is sufficient to consider only the rotationally symmetrical terms with index m=0 of the intensity point-spread function. However, in practice, nonrotationally symmetric effects occur. As an example, mechanical X- and Y-position noise do not need to have the same amplitude, because the mechanical construction of a wafer stage is usually not symmetrical in X and Y. In addition, 1-D synchronization errors may occur for a wafer scanner. Although the underlying cause is mechanical, these effects can be modeled as "anisotropic diffusion" with a Gaussian blurring kernel that is no longer rotationally symmetric, i.e., with σ_x- and σ_y-values that are unequal. Anisotropic diffusion has a preferential direction that causes an elliptical deformation of the PSF, and has an even

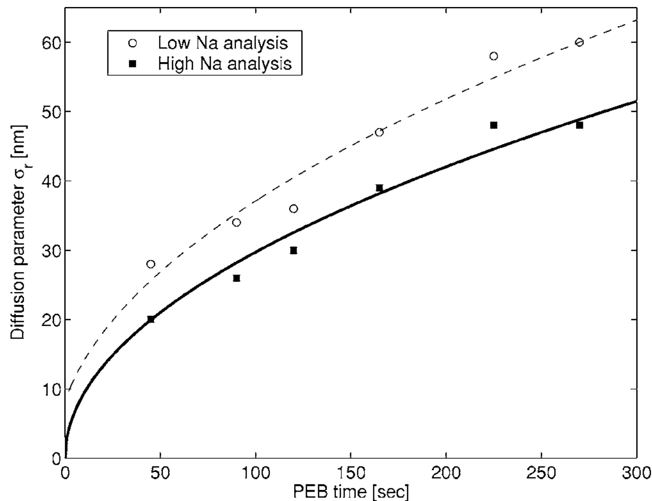

Fig. 10 The measured diffusion parameter σ_r versus the PEB time for the GARS-8105 resist. The open circles represent the σ_r values obtained by the low-NA analysis. The closed square symbols represent the σ_r values obtained by the high-NA analysis. The lines represent a data fit to a $\sqrt{2D\cdot t+\text{offset}}$ diffusion law. Note that the fitted curve for the high-NA case (solid line) passes nearly through the origin. The exposures are made on an ASML PAS5500/1150 with a $\lambda=193$ nm, NA=0.75 projection lens, unpolarized illumination.

through-focus dependence. To describe the effects of anisotropic diffusion on the PSF, we need to consider the second Fourier component with coefficients $\beta_{2p,2}$, with $p=1,2,\ldots$. In a way similar to Eq. (15), we can define a figure of merit $M(\sigma_x,\sigma_y)$ that expresses the relative power in the coefficients $\text{Re}(\beta_{2p,2})$. The minimum of the figure of merit corresponds to the anisotropic diffusion coefficients.

5.2 *Ultra-High Numerical Aperture Applications*

It was shown that a scalar analysis of the through-focus point-spread function according to the extended Nijboer-Zernike theory allows aberration retrieval and retrieval of the parameters of the extended DAIM model, i.e., the diffusion parameter and the focus noise parameter. However, the applicability of the scalar analysis is limited to systems with an NA value up to 0.65.

For systems with a high value of the numerical aperture, the basic methods employed in the previous scalar approach can still serve as a starting point for the high-NA analysis.[24–26] The procedure to retrieve the aberrations of a high-NA imaging system is based on the vectorial analysis of aberrated imaging systems. This procedure applies, for example, also to water-immersion systems that may have NA value as high as 1.35. It can be shown that one needs an analysis of the through-focus intensity point-spread function for typically four incident states of polarization to enable the retrieval of the vectorial pupil function, which also includes the effects of birefringence induced by the imaging system. In the case of a high-NA optical system that uses natural, unpolarized light, the retrieval scheme for aberrations and DAIM parameters simplifies considerably and is quite similar to that of the low-NA scalar retrieval scheme.[26]

Figure 10 shows the measured diffusion parameter σ_r versus the PEB time for GARS-8105 resist (Fuji Film) and compares the results obtained by the scalar low-NA analysis and the high-NA analysis for natural light. In both cases, we observe the expected increase of σ_r in time, caused by acid diffusion. The data fit, indicated by the dashed lines, represents a $\sqrt{2D\cdot t+\text{offset}}$ function. The low-NA analysis shows an offset. In contrast, the high-NA analysis shows a nearly zero offset. The offset reduction is caused by the fact that the basic intensity functions that we use for the high-NA analysis are now calculated by the full, vectorial ENZ theory, and have a somewhat larger halfwidth compared to the basic intensity functions from the scalar theory.

6 Summary

We present a method to determine the parameters of the extended DAIM model: the diffusion parameter, the focus noise parameter, and the aberrations of the projection lens. All parameters are derived from a single experiment. The mathematical framework is the extended Nijboer-Zernike theory that describes the point-spread function in the presence of diffusion and focus noise. The analysis to retrieve the parameters has been validated by simulations and experiments. The advantage of our approach is a clear separation between the optical parameters like pattern size, illuminator, projection lens aberrations on the one hand, and resist parameters on the other. Our method can be extended to optical systems with very high numerical aperture.

Acknowledgments

Philips Research Leuven makes use of the cleanroom facilities of IMEC, Leuven, Belgium. The support of the IMEC litho and etch departments, as well as from the IMEC P-Line is greatly appreciated. This work is partly sponsored through the Excite MEDEA+T406 project. The authors wish to thank Hans Kwinten, David Van Steenwinckel from Philips Research Leuven, and Ad Leeuwestein from Philips Research Eindhoven for the helpful discussions and careful reading of the manuscript.

Appendix A: Normalization of the Coordinates

The relationship between normalized image coordinates (x,y) and the defocus parameter f on the one hand, and the real space image coordinates (X,Y,Z) in the lateral and axial direction on the other, is given by

$$x=X\frac{\text{NA}}{\lambda},\quad =Y\frac{\text{NA}}{\lambda},\quad f=2\frac{\pi}{\lambda}Z(1-\sqrt{1-\text{NA}^2}). \tag{16}$$

Furthermore, we have $(x,y)=(r\cos\phi, r\sin\phi)$ with (r,ϕ) polar coordinates in the image plane.

Appendix B: *V* Functions and the Correction for the Finite Hole Size

The point-spread function or impulse response[21] of an optical system is the image of an infinitely small object. In practice, an object having a diameter of the order of $\lambda/2\text{NA}$ can still be regarded as infinitely small. The extended Nijboer-Zernike theory is used to calculate the complex amplitude of the through-focus point-spread function. This calculation involves the functions $V_n^m(r,f)$, given in integral form as

$$V_n^m(r,f) = \int_0^1 \exp(if\rho^2) R_n^m(\rho) J_m(2\pi\rho r)\rho d\rho, \tag{17}$$

with R_n^m being the Zernike polynomials and J_m the Bessel functions of the first kind. Here we have integers $n,m \geqslant 0$ with $n-m \geqslant 0$ and even. For such integers n,m, we have, setting $p=(n-m)/2$ and $q=(n+m)/2$, the Bessel series representation

$$V_n^m(r,f) = \exp(if) \sum_{l=1}^{\infty} (-2if)^{l-1} \sum_{j=0}^{p} v_{lj} \frac{J_{m+l+2j}(v)}{lv^l}, \tag{18}$$

with $v=2\pi r$. The v_{lj} are given for $l=1,2,\ldots$ and $j=0,\ldots,p$ by

$$v_{lj} = (-1)^p (m+l+2j) \binom{m+j+l-1}{l-1} \binom{j+l-1}{l-1} \times \binom{l-1}{p-j} \Big/ \binom{q+l+j}{l}. \tag{19}$$

As a rule of thumb, we have (see Ref. 11, Appendix B) that sufficient accuracy is obtained when the infinite series over l is truncated at $l=3|f|$.

It is advantageous to use holes with a non-negligible diameter, since the increased amount of light reduces the required exposure dose significantly, making the experimental procedure much more practical. We assume that the diameter is small compared to the coherence radius of the illumination source, a condition that is almost always satisfied. A non-negligible diameter of the object hole causes a nonuniform far-field pattern that results in drop-in amplitude at the rim of the pupil. The extended Nijboer-Zernike theory is sufficiently flexible to account for this effect, with amplitude drops as large as 50%. The $V_n^m(r,f)$ of Eq. (18) should be replaced throughout by

$$\exp(c) V_n^m(r,f+id). \tag{20}$$

As one can see from Eq. (18), nothing prevents us from using the Bessel series representation with complex defocus parameter $f+id$. The optimal c,d in Eq. (20) are accurately given as a function of $b=2\pi a$ by

$$c = \frac{b^4}{2304} + \frac{b^6}{46080}, \quad d = \frac{b^2}{8} + \frac{b^4}{384} + \frac{b^6}{10240}, \tag{21}$$

with a the normalized diameter of the hole. For details we refer to Ref. 13 (see Ref. 23 for an alternative method).

Appendix C: Correcting the Basic Functions for Spatial Diffusion and Focal Stochastics

In the main text, we require the convolution of the basic functions Ψ_n^m and χ_n^m, with the function $d(x,y)$ of Eq. (5) in the image planes and with f_n of Eq. (9) in the focal direction.

In this appendix, we develop first-order approximations for the cases $m=0$, $n=2p$, $p=1,2,\ldots$, and second-order approximations for the case $m=0$, $n=0$ for the combined effect of the two convolutions. We consider more general, radially symmetrical functions

$$W(x,y;f;t,s) \equiv W(r;f;t,s), \tag{22}$$

in which (x,y), r are the spatial Cartesian, radial coordinates, f is the focal parameter, and $t \geqslant 0$ and $s \geqslant 0$ are interpreted as diffusion time for the diffusion in the image planes and the smearing in the focal direction, according to the probability density function (pdf) in Eqs. (5) and (9), respectively. By Taylor expansion around $t=s=0$, we have

$$\begin{aligned} W(r;f;t,s) = {} & W(r;f;0,0) + t\frac{\partial W}{\partial t}(r;f;0,0) + s\frac{\partial W}{\partial s}(r;f;0,0) \\ & + \frac{1}{2}t^2 \frac{\partial^2 W}{\partial t^2}(r;f;0,0) + ts\frac{\partial^2 W}{\partial t \partial s}(r;f;0,0) \\ & + \frac{1}{2}s^2 \frac{\partial^2 W}{\partial s^2}(r;f;0,0) + \cdots . \end{aligned} \tag{23}$$

With D, c being the diffusion constants for the diffusion in the image planes and the smearing in the focal direction, we have

$$\frac{\partial W}{\partial t} = D\left(\frac{\partial^2}{\partial x^2} + \frac{\partial^2}{\partial y^2}\right) W, \quad \frac{\partial W}{\partial s} = c\frac{\partial^2 W}{\partial f^2}. \tag{24}$$

For $t,s>0$, the function $W(r;f;t,s)$ can be expressed in terms of $W(r;f;0,0)$ as

$$\begin{aligned} W(r;f;t,s) = {} & \int_{-\infty}^{\infty}\int_{-\infty}^{\infty}\int_{-\infty}^{\infty} \frac{1}{4\pi tD} \exp\left\{-\frac{1}{4tD}[(x-x')^2 \right. \\ & \left. + (y-y')^2]\right\} \frac{1}{\sqrt{4\pi sc}} \exp\left[-\frac{1}{4sc}(f-f')^2\right] \\ & \times W(x',y';f';0,0)\mathrm{d}x'\mathrm{d}y'\mathrm{d}f'. \end{aligned} \tag{25}$$

We thus get the integral kernels in Eqs. (5) and (9) by choosing t,s such that $\sigma_r=\sqrt{2Dt}$, $\sigma_f=\sqrt{2cs}$.

Instead of calculating the convolutions in Eq. (25) numerically, we compute the approximations of $W(r;f;t,s)$ using Eqs. (23) and (24). For $W=\chi_{2p}^0$, ψ_{2p}^0 with $p=1,2\ldots$, it is enough to include the first-order correction terms. Thus, recalling that $\sigma_r=\sqrt{2Dt}$, $\sigma_f=\sqrt{2cs}$, we approximate the diffused-and-smeared W for these cases as

$$\begin{aligned} & W(r;f;0,0) + \frac{1}{2}\sigma_r^2\left(\frac{\partial^2}{\partial x^2} + \frac{\partial^2}{\partial y^2}\right)W(r;f;0,0) \\ & + \frac{1}{2}\sigma_f^2 \frac{\partial^2}{\partial^2 f}W(r;f;0,0). \end{aligned} \tag{26}$$

For the case that $p=0$, the correction per Eq. (26) is sometimes not sufficiently accurate due to the relatively large amount of spatial diffusion. It is then necessary to include the first term in the second line of Eq. (23) into the correction, the other two terms being smaller. Then the diffused-and-smeared $W=|V_{0,0}|^2$ is approximated as

$$W(r;f;0,0)+\frac{1}{2}\sigma_r^2\left(\frac{\partial^2}{\partial x^2}+\frac{\partial^2}{\partial y^2}\right)W(r;f;0,0)$$
$$+\frac{1}{2}\sigma_f^2\frac{\partial^2}{\partial^2 f}W(r;f;0,0)+\frac{1}{8}\sigma_r^4\left(\frac{\partial^2}{\partial x^2}+\frac{\partial^2}{\partial y^2}\right)^2 W(r;f;0,0). \quad (27)$$

From Eq. (3) we then see that we need to compute

$$\left(\frac{\partial^2}{\partial x^2}+\frac{\partial^2}{\partial y^2}\right)(V_{2p}^0V_0^{0*}), \quad \frac{\partial^2}{\partial f^2}(V_{2p}^0V_0^{0*}), \quad (28)$$

for $p=0,1,\ldots$, and in addition for $p=0$

$$\left(\frac{\partial^2}{\partial x^2}+\frac{\partial^2}{\partial y^2}\right)^2|V_0^0|^2. \quad (29)$$

For this we have the following results

$$\frac{1}{2\pi^2}\left[\frac{\partial^2}{\partial x^2}+\frac{\partial^2}{\partial y^2}\right]V_{2p}^0V_0^{0*}=-\left(\frac{p+1}{2p+1}V_{2p+2}^0+2V_{2p}^0+\frac{p}{2p+1}V_{2p-2}^0\right)V_0^{0*}-V_{2p}^0V_2^{0*}+4\left(\frac{p+1}{2p+1}V_{2p+1}^1+\frac{p}{2p+1}V_{2p-1}^1\right)V_1^{1*}, \quad (30)$$

with the special result

$$\frac{1}{2\pi^2}\left(\frac{\partial^2}{\partial x^2}+\frac{\partial^2}{\partial y^2}\right)|V_0^0|^2=-2|V_0^0|^2+4|V_1^1|^2-2\,\mathrm{Re}(V_2^0V_0^{0*}) \quad (31)$$

for $p=0$. Next we have

$$-\frac{\partial^2 V_{2p}^0V_0^{0*}}{\partial f^2}=\frac{(p+1)(p+2)}{4(2p+1)(2p+3)}V_{2p+4}^0V_0^{0*}+\frac{\frac{5}{6}p^2+\frac{5}{6}p-\frac{1}{2}}{(2p-1)(2p+3)}V_{2p}^0V_0^{0*}+\frac{p(p-1)}{4(2p-1)(2p+1)}V_{2p-4}^0V_0^{0*}-\frac{p+1}{2(2p+1)}V_{2p+2}^0V_2^{0*}-\frac{p}{2(2p+1)}V_{2p-2}^0V_2^{0*}+\frac{1}{6}V_{2p}^0V_4^{0*}, \quad (32)$$

with the special result

$$\frac{\partial^2}{\partial f^2}|V_0^0|^2=-\frac{1}{6}|V_0^0|^2+\frac{1}{2}|V_2^0|^2-\frac{1}{3}\,\mathrm{Re}(V_4^0V_0^{0*}), \quad (33)$$

for the case $p=0$. Finally, there holds

$$\left[\frac{1}{2\pi^2}\left(\frac{\partial^2}{\partial x^2}+\frac{\partial^2}{\partial y^2}\right)\right]^2|V_0^0|^2=\frac{20}{3}|V_0^0|^2+4|V_2^0|^2-\frac{64}{3}|V_1^1|^2+8|V_2^2|^2+\mathrm{Re}\left[12V_2^0V_0^{0*}+\frac{4}{3}V_4^0V_0^{0*}-\frac{32}{3}V_3^1V_1^{1*}\right]. \quad (34)$$

The proof of all this uses the integral representation in Eq. (17), the fact that the Laplacian $\partial^2/\partial x^2+\partial^2/\partial y^2$ assumes the form $\partial^2/\partial r^2+1/r\cdot\partial/\partial r$ in polar coordinates for radially symmetric functions, Newton's binomium for differentiation of product functions, the fact that the differential equation

$$z^2J''(z)+zJ'(z)=(m^2-z^2)J(z) \quad (35)$$

is satisfied by J_m, the relation

$$\frac{m}{z}J_m(z)=1/2J_{m-1}(z)+1/2J_{m+1}(z), \quad (36)$$

and the fact that $\rho R_n^m(\rho)$ and $\rho^2R_n^m(\rho)$ can be written explicitly as a linear combination of Zernike polynomials with the upper index $m\pm1$ and m, respectively. For the $\partial^2/\partial f^2$ operator, the proof is similar, and in fact somewhat simpler.

For the sake of completeness, we mention that we have also analytical results for the two other terms on the second and third line of Eq. (23). There holds

$$\frac{1}{2\pi^2}\left(\frac{\partial^2}{\partial x^2}+\frac{\partial^2}{\partial y^2}\right)\frac{\partial^2}{\partial f^2}|V_0^0|^2=\frac{1}{3}|V_0^0|^2-|V_2^0|^2-\frac{4}{9}|V_1^1|^2+\frac{8}{9}|V_3^1|^2+\mathrm{Re}\left[\left(\frac{2}{15}V_2^0+\frac{2}{3}V_4^0+\frac{1}{5}V_6^0\right)V_0^{0*}-\frac{1}{3}V_4^0V_2^{0*}+\left(\frac{16}{45}V_3^1-\frac{4}{5}V_5^1\right)V_1^{1*}\right], \quad (37)$$

and

$$\frac{\partial^4}{\partial f^4}|V_0^0|^2=\frac{1}{15}|V_0^0|^2-\frac{3}{10}|V_2^0|^2+\frac{1}{6}|V_4^0|^2+\mathrm{Re}\left[\left(\frac{5}{21}V_4^0+\frac{1}{35}V_8^0\right)V_0^{0*}-\frac{1}{5}V_6^0V_2^{0*}\right], \quad (38)$$

for the last two terms on the right-hand side of Eq. (23), respectively [also see Eq. (24)]. Using Eqs. (23) and (24) and $\sigma_r=\sqrt{2Dt}$, $\sigma_f=\sqrt{2cs}$, the fully second-order corrected expression for $|V_0^0|^2$ becomes

$$|V_0^0|^2 + \pi^2\sigma_r^2[\text{RHS of Eq.}(31)] + \frac{1}{2}\sigma_f^2[\text{RHS of Eq.}(33)] + \frac{1}{2}\pi^4\sigma_r^4[\text{RHS of Eq.}(34)] + \frac{1}{2}\pi^2\sigma_r^2\sigma_f^2[\text{RHS of Eq.}(37)] + \frac{1}{8}\sigma_f^4[\text{RHS of Eq.}(38)], \quad (39)$$

where we have abbreviated RHS for right-hand side.

Much of what has been given for the special cases $m=0$, $n=2p$ can applied to the general (m,n) case as well.

References

1. D. Van Steenwinckel, H. Kwinten, S. Locorotondo, and S. Beckx, "Overbake: sub-40 nm gate patterning with ArF lithography and binary masks," *Proc. SPIE* **5376**, 215–225 (2004).
2. A. W. Lohmann and D. P. Paris, "Influence of longitudinal vibrations on image quality," *Appl. Opt.* **4**, 393 (1965).
3. J. Bischoff, W. Henke, J. V. D. Werf, and P. Dirksen, "Simulations on step and scan optical lithography," *Proc. SPIE* **2197**, 953–964 (1994).
4. D. G. Flagello, J. Mulkens, and C. Wagner, "Optical lithography into the millennium: Sensitivity to aberration, vibrations and polarization," *Proc. SPIE* **4000**, 172–183 (2000).
5. I. Lalovic, A. Kroyan, H. Liu, and H. J. Levinson, "Image-blur tolerances for 65 nm and 45 nm-node IC manufacturing," *Proc. SPIE* **5040**, 1570–1580 (2003).
6. J. Garofalo, J. DeMarco, J. Bailey, X. Xiao, and S. Vaidya, "Reduction of ASIC gate-Level line-end shortening by mask compensation," *Proc. SPIE* **2440**, 171–183 (1995).
7. C. N. Ahn, H. B. Kim, and K. H. Baik, "A novel approximate model for resist processing," *Proc. SPIE* **3334**, 752–763 (1998).
8. D. Fuard, M. Besacier, and P. Schiavone, "Assessment of different simplified resist models," *Proc. SPIE* **4691**, 1266–1277 (2002).
9. D. Fuard, M. Besacier, and P. Schiavone, "Validity of the diffused aerial image model: an assessment based on multiple test cases," *Proc. SPIE* **5040**, 1536–1543 (2003).
10. A. J. E. M. Janssen, "Extended Nijboer-Zernike approach for the computation of optical point-spread functions," *J. Opt. Soc. Am. A* **19**, 849 (2002).
11. J. J. M. Braat, P. Dirksen, and A. J. E. M. Janssen, "Assessment of an extended Nijboer-Zernike approach for the computation of optical point-spread functions," *J. Opt. Soc. Am. A* **19**, 858 (2002).
12. P. Dirksen, J. Braat, A. Janssen, C. Juffermans, and A. Leeuwestein, "Experimental determination of lens aberrations from the intensity point-spread function in the focal region," *Proc. SPIE* **5040**, 1–10 (2003).
13. P. Dirksen, J. Braat, A. J. E. M. Janssen, and C. Juffermans, "Aberration retrieval using the extended Nijboer-Zernike approach," *J. Microlithogr., Microfabr., Microsyst.* **2**(1), 61 (2003).
14. P. Dirksen, J. Braat, A. J. E. M. Janssen, A. Leeuwestein, H. Kwinten, and D. Van Steenwinckel, "Determination of resist parameters using the extended Nijboer-Zernike theory," *Proc. SPIE* **5377**, 150–159 (2004).
15. W. Hinsberg, F. Houle, M. Sanchez, J. Hoffnagle, G. Wallraff, D. Medeiros, G. Gallatin, and J. Cobb, "Extendibility of chemically amplified resists: Another brick wall?" *Proc. SPIE* **5039**, 1–14 (2003).
16. A. Erdmann, W. Henke, S. Robertson, E. Richter, B. Tollkhn, and W. Hoppe, "Comparison of simulation approaches for chemically amplified resists," *Proc. SPIE* **4404**, 99–110 (2001).
17. T. Brunner and R. Ferguson, "Approximate models for resist processing effects," *Proc. SPIE* **2726**, 198–207 (1996).
18. P. Graupner, A. Gohnermeier, M. Lowisch, P. Garreis, D. Flagello, S. Hansen, R. Socha, and C. Kohler, "Solutions for printing sub 100 nm contacts with ArF," *Proc. SPIE* **4691**, 503–514 (2002).
19. D. Van Steenwinckel, J. H. Lammers, T. Koehler, R. L. Brainard, and P. Trefonas, "Resist effects at small pitches," *J. Vac. Sci. Technol. B* (in press).
20. D. van Steenwinckel, J. H. Lammers, L. H. A. Leunissen, and J. A. J. M. Kwinten, "Lithographic importance of acid diffusion in chemically amplified resists," *Proc. SPIE* **5753**, 269–280 (2005).
21. M. Born and E. Wolf, *Principles of Optics*, 7th rev. ed., Sec. 8.8 Cambridge University Press, Cambridge, MA (2001).
22. C. van der Avoort, J. J. M. Braat, P. Dirksen, and A. J. E. M. Janssen, "Aberration retrieval from the intensity point-spread function in the focal region using the extended Nijboer-Zernike approach," *J. Mod. Opt.* **52**, 1695 (2005).
23. SOLID-C (release 6.3.0), SIGMA-C GmbH, Thomas-Dehlerstrasze 9, D-81737 Munich, Germany.
24. J. J. M. Braat, P. Dirksen, A. J. E. M. Janssen, and A. S. van de Nes, "Extended Nijboer-Zernike representation of the vector field in the focal region of an aberrated high-aperture optical system," *J. Opt. Soc. Am. A* **20**, 2281 (2003).
25. J. J. M. Braat, P. Dirksen, A. J. E. M. Janssen, and A. S. van de Nes, "Extended Nijboer-Zernike approach to aberration and birefringence retrieval in a high-aperture optical system," *J. Opt. Soc. Am. A* (in press).
26. P. Dirksen, J. J. M. Braat, A. J. E. M. Janssen, and A. Leeuwestein, "Aberration retrieval for high-NA optical systems using the extended Nijboer-Zernike theory," *Proc. SPIE* **5754**, 262–273 (2005).
27. See http://www.nijboerzernike.nl.

Peter Dirksen obtained his PhD degree in physics at Leiden University, Leiden, The Netherlands, in 1989. In 1990 he joined Philips Research Laboratories, Eindhoven, where he worked in several areas in optical lithography, including the field of alignment and exposure tool characterization.

Joseph Braat studied physics at Delft University of Technology and obtained his PhD at the Institut d' Optique Théorique et Appliquée in France in 1972. At Philips Research Laboratories, he worked on diffraction theory, optical disk systems, and optical lithography. In 1998 he became a professor of optics at Delft University of Technology, The Netherlands. He is a member of the Royal Netherlands Academy of Arts and Sciences and president of the European Optical Society.

Augustus J.E.M. Janssen received his PhD degree in mathematics from the Eindhoven University of Technology, Eindhoven, The Netherlands, in June 1979. From 1979 to 1981, he was a Bateman Research Instructor at the Mathematics Department of California Institute of Technology, Pasadena, California. In 1981 he joined Philips Research Laboratories, Eindhoven, where his principal responsibility is to provide high-level mathematical service and consultancy in mathematical analysis. Since 1999 he has been a research fellow of Philips Research Laboratories, Eindhoven, and in 2003 he was elected Fellow of the IEEE.